Experiments in Fluids (2019) 60:110
https://doi.org/10.1007/s00348-019-2753-y

RESEARCH ARTICLE

High frequency temperature fluctuation measurements by Rayleigh scattering and constant-voltage cold-wire techniques

Bertrand Mercier[1] · Emmanuel Jondeau[1] · Thomas Castelain[2] · Yuta Ozawa[3] · Christophe Bailly[1] · Geneviève Comte-Bellot[1]

Received: 14 February 2019 / Revised: 17 May 2019 / Accepted: 27 May 2019

Abstract

The thermal inertia of sensors drastically limits the measurement of the temperature fluctuations in the high-frequency range. This issue is often addressed using cold wire techniques with dedicated corrections. In this study, three methods are employed to compensate high-frequency attenuation, and the correction of the end losses, are evaluated for four wires with different aspect ratios and diameters. The fidelity of the corrected measurements is assessed by comparing the spectra of temperature fluctuations obtained with the cold wires operating in a constant voltage circuit, to those derived from optical measurements. The latter method is based on Rayleigh scattering and is in principle not affected by thermal inertia as it relies on molecular light scattering. Two flows presenting high levels of temperature fluctuations are considered. Namely, the wake of a heated cylinder, and a mixing layer between two jets in co-flow and at different temperatures. These two configurations allow exploring cold wire performances at high frequency, and show that precise measurements can be performed up to 10 kHz with a wire 1 µm in diameter.

Graphic abstract

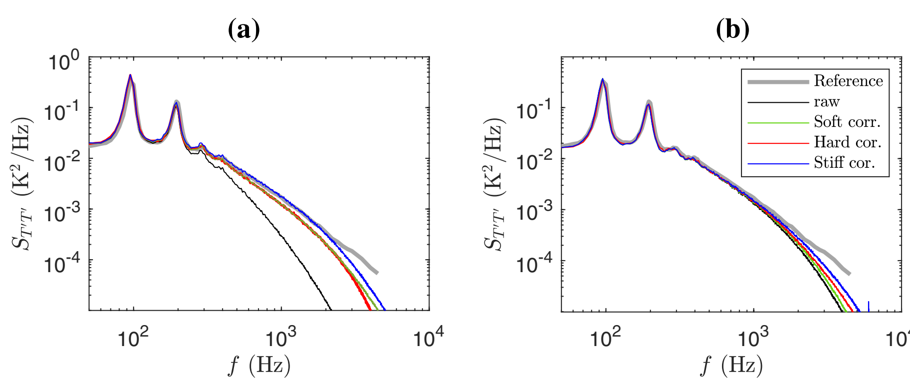

1 Introduction

The measurement of temperature fluctuations remains a challenging topic in thermoacoustics (Berson et al. 2010; Penelet et al. 2016; Cleve et al. 2017) and heat transport in turbulent flows (Sohn 1991; Panda 2016), for instance. Time resolved temperature measurements are often performed using cold wires for air flows. This type of probe is made of a metal wire with a resistance offering a large temperature coefficient. The measure of the local flow temperature is achieved indirectly by measuring the value of the wire resistance, assuming heat

✉ Bertrand Mercier
b.h.mercier@tudelft.nl

1 Univ Lyon, École Centrale de Lyon, INSA Lyon, Université Claude Bernard Lyon I, CNRS, LMFA, UMR 5509, 69134 Écully, France

2 Univ Lyon, Université Claude Bernard Lyon I, École Centrale de Lyon, INSA Lyon, CNRS, LMFA, UMR 5509, 69622 Villeurbanne, France

3 Experimental Aerodynamics Laboratory, Department of Aerospace Engineering, Tohoku University, Sendai, Japan

Published online: 10 June 2019

transfers lead to thermal equilibrium between the flow and the wire. Nevertheless, this process is affected by thermal inertia due to the wire's heat capacity, in particular when temperature fluctuations at high frequency are considered. Methods for recovering the high-frequency attenuation due to thermal lag have been studied extensively (LaRue et al. 1975; Antonia et al. 1981; Tsuji et al. 1992; Denos and Sieverding 1997; Berson et al. 2010; Cleve et al. 2017). However, the literature lacks quantitative analyses that thoroughly validate these corrections. This is mostly due to the need for a reliable method capable of measuring the high-frequency temperature fluctuations. In this study, the results obtained from a Rayleigh scattering based method that allows measuring the density from which the temperature fluctuations can be deduced are used as a reference for comparison with other techniques. The Rayleigh scattering measurement relies on laser light scattered by the molecules constituting the flow itself. This method has proven its reliability in many supersonic and subsonic flows for density measurements (Panda and Seasholtz 2002; Panda and Gomez 2003; Panda et al. 2005; Panda 2016; Mercier et al. 2018b, a). The conversion from density to temperature relies on the perfect gas law under the hypothesis of an isobar flow. Two low-speed open flows are considered in the following and described in Sect. 4. In particular, the first flow is chosen because it contains strong temperature fluctuations at low frequencies in comparison with the cut-off frequency due to the thermal inertia of the wire. The wake of a heated cylinder was selected for this purpose. The second flow is the mixing layer of a hot jet in cold surroundings in which significant temperature fluctuations are generated at a frequency up to 10 kHz, which is a suitable flow to assess the cold wire technique performances. Following the description of the experimental configurations, Sect. 5 is dedicated to the analysis of the results with the comparison of three different thermal inertia compensation methods and the analysis of the effect of the wire aspect ratio on the measurement of temperature fluctuations. Descriptions of the Rayleigh scattering and the cold wire measurement techniques are provided in Sects. 2 and 3, respectively.

2 Rayleigh scattering measurement

2.1 Principles

The Rayleigh scattering method used for the present study relies on the elastic scattering of light by the molecules constituting the flow to be probed. For an incident laser light of irradiance I, the power P_s of the light scattered by the molecules contained in a probed volume V_{sc} in the direction of an observer covering a solid angle $d\Omega$ is given by:

$$P_s = \frac{\rho N_A}{\mathcal{M}} V_{sc} \frac{\partial\sigma}{\partial\Omega} d\Omega \sin^2(\psi) I, \tag{1}$$

where ρ, N_A and $\mathcal{M}$ are the density, the Avogadro constant and the molar mass of air, and $\partial\sigma/\partial\Omega$ is the differential scattering cross-section which corresponds to the ability of a given molecule to scatter light of a given wavelength. For diatomic molecules like dioxygen and dinitrogen, $\partial\sigma/\partial\Omega$ depends little on the direction of the observation, but for the purpose of this study $\partial\sigma/\partial\Omega$ is assumed to be isotropic. Directivity with the angle Ψ between the observer and the plane of the light polarization is simply introduced. More details on the principle and practical applications of this method can be found for instance in Panda and Seasholtz (2002), Panda and Gomez (2003), Mercier et al. (2018a, b). From Eq. (1), and for the present experimental setup, $P_s \sim 10^{-11}$ W (Mercier et al. 2018b). This power is too small to be measured directly with a light power meter. Thus, it is more convenient to consider the power as a flux of photons of energy hc/λ with h being the Planck constant, c the speed of light, and λ the light wavelength. The flux of photon ϕ_d detected by a photon-detector device, in this case a photomultiplier, is, therefore, given by

$$\Phi_d = Q_E \frac{\lambda}{hc} \frac{\rho N_A}{\mathcal{M}} V_{sc} \frac{\partial\sigma}{\partial\Omega} d\Omega \sin^2(\psi) I. \tag{2}$$

The quantum efficiency Q_E is introduced to take into account the probability of a photomultiplier to detect a photon arrival. Typically, the value $\Phi_d \sim 10^8$ photon/s is observed with the present bench (Mercier et al. 2018b). In the context of the experiments described in Panda and Seasholtz (2002), Panda and Gomez (2003), Mercier et al. (2018a, b) given as examples, all the parameters of Eq. (2) remain constant throughout the test campaign except the density ρ. All these parameters can, therefore, be represented by a constant k determined through a calibration process leading to

$$\Phi_d = k\rho + \Phi_{amb}. \tag{3}$$

The calibration process, detailed in the next section, requires the introduction of the new term Φ_{amb} because a photon flux corresponding to the ambient stray light is also measured despite efforts to keep its level as low as possible. Equation (3) now allows determining the density from the photon flux.

2.2 Photon flux

The counted photon flux Φ_c is estimated by counting the number of photon arrivals N during the time interval Δt; hence $\Phi_c = N/\Delta t$ or $\Phi_c = Nf_s$. The time history of the photon flux is hence obtained by repeating this counting over the successive time intervals. However, two difficulties arise when photon counting methods are employed. First, this estimation suffers from a bias that turns into an uncertainty because photon arrivals are discrete events randomly

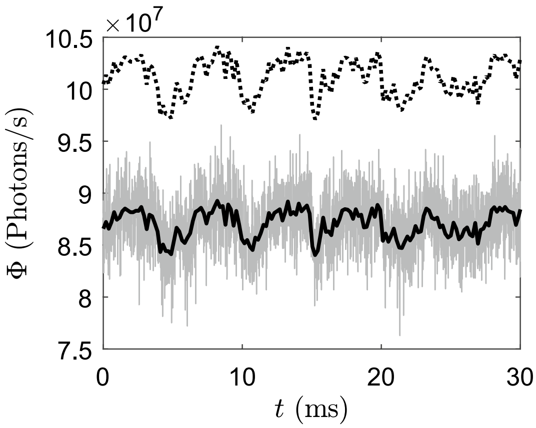

Fig. 1 Flux of photons Φ_c (uncorrected) and Φ_d (corrected from pileup) collected from a heated cylinder wake. Grey line $f_s = 100$ kHz, Black line $f_s = 5$ kHz, Dotted line $f_s = 5$ kHz corrected from pileup

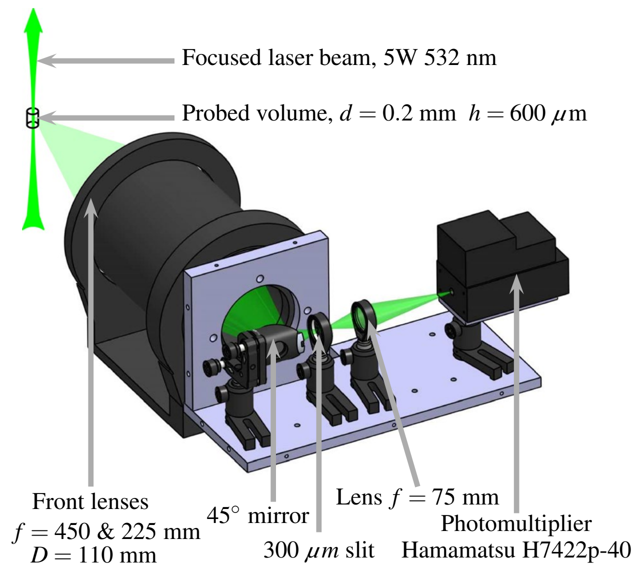

Fig. 2 CAD sketch of the light collector

distributed in time. Their distribution follows a Poisson's law. This uncertainty is reduced for a larger Δt, or larger photon fluxes, but still exists and consists of a noise, called shot noise, in the resulting $\Phi_c(t)$ signals. This property of the shot noise can be observed in Fig. 1 that depicts the photon flux measured from a point in the wake of a heated cylinder. The photon flux sampled at $f_s = 5$ kHz clearly shows the effect of the vortex shedding onto the flow density, thus the photon flux. However, for the sampling frequency $f_s = 100$ kHz, the noise contribution makes it difficult to interpret $\Phi_c(t)$ due to the smaller Δt and thus the higher shot noise contribution.

The random arrival of photons induces a second bias, known as the pileup effect. It is linked to the probability that two photons are detected at the same time. When simultaneous detections occur, only one can be counted instead of two. That is why in the present section the flux of photons is denoted by Φ_c, for counted, while in the previous section it was denoted by Φ_d, for detected. This bias increases with the photon flux and induces a non-linearity between Φ_c and ρ. The time distribution of the photon arrival is dictated by Poisson's law from which a compensation formula can be derived (Mercier et al. 2018b):

$$\Phi_d = \frac{\Phi_c}{1 - \tau\Phi_c}, \tag{4}$$

where τ is the pulse pair resolution of the acquisition system that corresponds to the minimum time delay for two detections to be counted. With the present system, the value $\tau = 1.6$ ns was determined previously (Mercier 2017). The photon flux Φ_d resulting from this correction is plotted by a dashed line in Fig. 1. The corrected flux Φ_d is larger than the counted photon flux Φ_c by approximately 15%.

2.3 Optical setup

The Rayleigh scattering measurement system consists of a light source, here a 5 W continuous 532 nm fiber laser, and a light collector shown in Fig. 2. There is a 300 µm slit in the light collector set perpendicular to the laser beam that defines the probed region. The latter is a cylinder whose diameter is the same as the laser beam diameter and with a height of 600 µm due to the magnification factor of the optical setup. The laser beam is focused near the probed region leading to a diameter estimated around 0.2 mm. The light collected from this region is focused onto a Hamamatsu H7422p-40 photomultiplier dedicated to photocounting applications. The output signal of the photomutiplier is sampled by a NI-1062 high-speed digitizer, and the time arrivals of all the individual photons are determined according to the method provided in Mercier et al. (2018b).

2.4 Calibration

The calibration process is performed in the potential core of a hot jet generated by a wind tunnel equipped with a heating system. The temperature of the flow can be raised to 80 °C and is monitored. Heating the flow to this temperature takes about 15 min. It was chosen here to measure the density for 0.86 s every 20 s simultaneously with the temperature for 30 min comprising a heating and a cooling phase. The density is deduced from the temperature and the atmospheric pressure which is also measured, and compared to the photon flux in Fig. 3. The calibration coefficients are deduced from the measured data with a linear fitting. The slope is 8.4×10^7 photons/(kg/m^3), with an

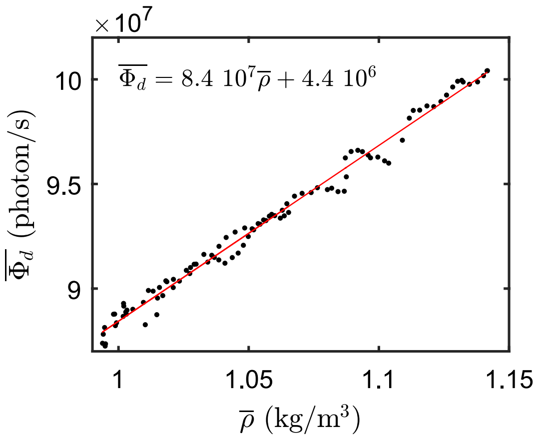

Fig. 3 Curve of calibration. black square result, red line linear fit

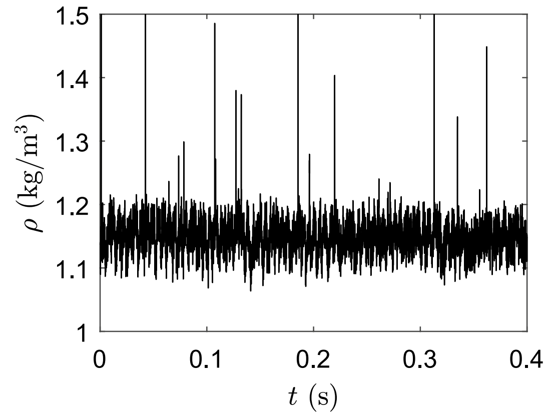

Fig. 4 Density signal sampled at 20 kHz with the signature of dust detection

uncertainty of ±2.4% considering a 95% confidence level and assuming a Gaussian distribution of the errors.

2.5 Software particle cleaning

In the context of this study, Rayleigh scattering refers to the light scattering by the molecules constituting the flow. However, air also contains particles with diameters much larger than molecules. According to the Rayleigh scattering theory, the scattering cross-section of a particle increases with the sixth power of its diameter. Indeed, a single dust particle of diameter 0.1 µm scatters the same amount of light as the 10^{14} molecules of diameter 0.3 nm contained in the probed volume. The presence of dust particles in the flow is thus strongly detrimental to the measurements. High efficiency air filters are set in the wind tunnel to drastically reduce the concentration of dust particles, but it is not possible to remove all particles as small as 0.1 µm. As a result, the density signals are affected by spikes of random amplitude as shown in Fig. 4.

A software-based method is applied here to reduce the noise arising from dust particle detections in the signal. It consists in estimating the standard deviation σ_ρ of the density signal, and in tagging all data above a threshold, i.e. $3\sigma_\rho$. The challenge lies in estimating the standard deviation of ρ from the corrupted signal. Many methods could be used, but that proposed in the following operates in any condition without tuning parameters. First, the average density $\overline{\rho^*}$ is computed from the corrupted signal. The bias due to dust detection signatures on the estimation of the averaged value $\overline{\rho^*}$ is assumed to be negligible because the dust detections are sparse in the signal. Noting that dust detection signatures consist of an excess of photons, it is, therefore, reasonable to consider that data below the average are not corrupted. The standard deviation is then simply calculated from

$$\sigma_\rho = \sqrt{\frac{1}{n}\sum_{i=1}^{n}\left(\rho_i - \overline{\rho^*}\right)^2}, \tag{5}$$

where ρ_i are the n values of ρ below the average. If necessary, $\overline{\rho^*}$ can be computed again only with data below the threshold of $3\sigma_\rho$, and the standard deviation is estimated with this new average until the value converges. Data above the threshold are tagged and can be replaced by the average value.

In practice, the sampling frequency f_s affects the efficiency of this treatment. If the sampling frequency is too low, the dust detection signature is composed of only one sample also likely to contain non-corrupted signals that would be revealed by increasing the sampling frequency to obtain a finer discretisation of the spike. On the contrary, if f_s is too large, the spike wings are flatter, and it becomes difficult to clearly identify the corrupted part of the signal (Mercier et al. 2018b). A suitable Δt for the sampling is found between 1/4 and 1/2 of the time of flight of the particle across the beam, meaning that the signatures are discretized by 2–4 samples. For the present study the convenient frequency is between 30 and 60 kHz according to the experimental configurations presented in the following, and less than 1% of the signal was corrupted.

Nonetheless, to compute the spectrum of the density fluctuation, a customized method described in the next section is used. It requires higher sampling frequencies to prevent the introduction of any bias in the spectrum. A solution employed here is to first sample the density at the ideal frequency for dust removal, then tag the corrupted data and store their corresponding times, and second, replace by the average value the corresponding data in the signal sampled at higher frequency.

The ability to sample signals at any desired frequency is derived from storing the arrival times of the photons rather than keeping a time history of the count rate.

2.6 Temperature fluctuation spectrum calculation

The density signal presented in Fig. 4 contains noise due to the shot noise. The shot noise is a white noise that in general represents a significant contribution to the total fluctuations of signals obtained from photo-counting. It turns into a noise floor in the density spectrum $S_{\rho'\rho'}$. Panda and Seasholtz (2002) proposed a method based on two photomultipliers to drastically reduce shot noise. Here, an adaptation of this method, which requires only one photomutliplier, and which has been proven to provide equivalent results in Mercier et al. (2018b) is used.

If the density signal is sampled at a high enough frequency, the contribution of the aerodynamic fluctuations ρ'_{A} will be coherent from one sample to the next, whereas the shot noise contribution ρ'_{SN} will be random and point to point independent. Then, the initial density signal $\rho(t)$ is split into $\rho_1(t)$ and $\rho_2(t)$ by taking one point out of two for the first $\rho_1(t)$, and the remaining points for $\rho_2(t)$. These resulting signals are sampled at half the initial sampling frequency. Contributions $\rho'_{1_{\mathrm{A}}}$ and $\rho'_{2_{\mathrm{A}}}$ are expected to be coherent, and contributions $\rho'_{1_{\mathrm{SN}}}$ and $\rho'_{2_{\mathrm{SN}}}$ are expected to be independent. The spectrum of the density fluctuations, thus of ρ'_{A}, can, therefore, be estimated by computing the cross-spectrum between $\rho_1(t)$ and $\rho_2(t)$ to reject the incoherent part, for instance with the periodogram method. Details on this method are provided in Mercier et al. (2018b).

At this stage, the density fluctuation spectrum $S_{\rho'\rho'}$ is known, and must be converted into a spectrum of temperature fluctuations $S_{T'T'}$. The differentiation of the ideal gas law, $p = \rho r T$ where $r = 287$ J/(kg K) for air and p is the static pressure, gives

$$\frac{\rho'}{\overline{\rho}} = \frac{p'}{\overline{p}} + \frac{T'}{\overline{T}}. \tag{6}$$

In the present experiment, the flows are especially chosen to promote temperature fluctuations. Besides, low-speed open flows are considered and hence flows with small pressure fluctuations. Pressure fluctuations can, therefore, be neglected in comparison to the temperature fluctuations (Panda 2016). Under this hypothesis, the temperature fluctuation spectrum $S_{T'T'}$ is

$$S_{T'T'} = \left(\frac{\overline{T}}{\overline{\rho}}\right)^2 S_{\rho'\rho'}. \tag{7}$$

3 Cold wire temperature measurement

3.1 Principles

Cold wire thermometry consists in using a wire at over-heat low enough to neglect the difference between the local temperature T_{a} and the wire temperature T_{w} in static conditions. The wire temperature is deduced from its electrical resistance R_{w} using:

$$R_{\mathrm{w}} = R_0\left(1 + \chi\left(T_{\mathrm{w}} - T_0\right)\right), \tag{8}$$

where R_0 is the resistance of the wire at temperature T_0, and χ is the temperature coefficient of the wire material. Under static conditions, the wire temperature is equal to the ambient temperature. However, under dynamic conditions, the thermal inertia causes a lag between T_{a} and T_{w}, also associated with an attenuation. Considering an ideal wire devoid of thermal inertia, the corresponding resistance R^*_w is given at any frequency by

$$R^*_{\mathrm{w}} = R_0\left(1 + \chi\left(T_{\mathrm{a}} - T_0\right)\right). \tag{9}$$

The relation between the resistance of a real and an ideal wire can be approximated for small fluctuations, following (Berson et al. 2010)

$$R^*_{\mathrm{w}} = R_{\mathrm{w}} + \mathscr{M}_{\mathrm{w}}\frac{\mathrm{d}R_{\mathrm{w}}}{\mathrm{d}t}, \tag{10}$$

or in terms of temperature

$$T_{\mathrm{a}} = T_{\mathrm{w}} + \mathscr{M}_{\mathrm{w}}\frac{\mathrm{d}T_{\mathrm{w}}}{\mathrm{d}t}, \tag{11}$$

where

$$\mathscr{M}_{\mathrm{w}} = \frac{m_{\mathrm{w}}c_{\mathrm{w}}}{\chi R_0}\frac{1}{f[U]}, \tag{12}$$

is the thermal lag of the wire, in seconds. This time is proportional to the quantity of heat in the wire equal to the product of the wire mass m_{w} by the specific heat of the wire c_{w}, divided by the rate of heat transfer by convection depending on the normal velocity U represented by $f[U]$.

3.2 Thermal inertia corrections

Applying the Fourier transform denoted $\mathscr{F}()$ to Eq. (10) gives

$$\mathscr{F}(R_{\mathrm{w}}) = \frac{\mathscr{F}(R^*_{\mathrm{w}})}{1 + \mathscr{M}_{\mathrm{w}} j\omega}. \tag{13}$$

This would be a first-order low-pass filter of cutoff frequency $f_{\mathrm{c}} = 1/(2\pi\mathscr{M}_{\mathrm{w}})$ if $\mathscr{M}_{\mathrm{w}}$ were constant in time.

In this study three methods of recovering R^*_w, hence obtaining T_{a} from R_{w}, are assessed. Two of them are discussed in detail in Cleve et al. (2017). All of them are based on measures acquired with a *Tao systems* prototype constant voltage anemometer (CVA) that controls the voltage at a constant value close to 6 mV across the wire with the aid of a feedback loop. The anemometer output signal is linearly related to the current through the wire, thus with the inverse of R_w. The first and second methods of recovering R_w^* are called hardware correction and software correction (Cleve et al. 2017), and the third is referred to as stiff software correction.

The hardware correction is directly implemented in the voltage control feedback loop. It consists in adding a zero in the transfer function, rolling on at the frequency $f_c = 1/(2\pi T_c)$. The time constant T_c is chosen from a set of discrete values defined by couples of resistors and capacitors. In parallel, $\mathscr{M}_w$ is assumed to be a constant and estimated by measuring the response time of the wire in flow conditions similar to that of the measurement. The nearest value of T_c to $\mathscr{M}_w$ is set in the anemometer to directly measure an estimation of R_w^*, and deduce T_a.

For the software correction, T_c is set to 0; indeed the correction is applied during the software processing of the anemometer output value to recover R_w^* (Mangalam 2018) by solving equation (10). In this configuration, $\mathscr{M}_w$ is determined from values of $(m_w c_w)/(\chi R_0)$ and $f[U]$ determined separately by calibration following methods proposed in Comte-Bellot et al. (2004), Cleve et al. (2017). The term $(m_w c_w)/(\chi R_0)$ is a constant for a given wire, whereas $f[U]$ is a function of the flow velocity. The major interest of this method is that $\mathscr{M}_w$ can be time-dependent provided the instantaneous velocity is known. To measure the velocity, a hot wire operated simultaneously by another constant voltage anemometer is set close to the cold wire. In principle, this second method should be more efficient than the first one because $\mathscr{M}_w$ varies in time. Consequently, this method is well suited for one-dimensional or two-dimensional flows, but difficulties appear in three-dimensional turbulent flows if their integral length scales are shorter than the distance between the wires.

The third correction is also software based, and simply consists in applying the same correction as the hardware correction, but during the post-processing by solving Eq. (10) with any arbitrarily chosen time constant instead of a preset value. This method is based on the same hypothesis as the hardware correction; hence there is a constant value in time for $\mathscr{M}_w$.

3.3 Correction of end heat losses

In Sects. 3.1 and 3.2, the wires were assumed to be of infinite length, meaning that the heat transfer between the wire and the prongs was not considered. The so-called thermal end losses are discussed comprehensively in Tsuji et al. (1992), Bruun (1995). The results can be summarized as follows: As the prongs are significantly bigger than the wires, the latter remain at the mean ambient temperature and impose a constant temperature boundary condition at both ends of the wire. A heat loss, therefore, occurs from the wire to the prongs, which decreases the temperature sensitivity of the wire. The temperature fluctuations are decreased by a factor H_p estimated by

$$H_p = 1 - 2\frac{l_c}{l}, \tag{14}$$

where l is the wire length, and l_c is the cold wire length, an effective length for the wire defined as (Bruun 1995)

$$l_c = 0.5d\sqrt{\frac{k_w}{k_f}\frac{1}{Nu}}, \tag{15}$$

with k_w and k_f being the thermal conductivity of the wire and fluid, and Nu the Nusselt number, here estimated from (Collis and Williams 1959)

$$Nu = 0.24 + 0.56Re^{0.45}. \tag{16}$$

The Reynolds number Re is based on the average normal flow velocity, on the wire diameter, and on the viscosity of the fluid at the average temperature.

Temperature spectra $S_{T'T'}$ are corrected from the end losses following

$$S_{T'T'} = \frac{S_{T'T'}^{\text{raw}}}{H_p^2}, \tag{17}$$

where $S_{T'T'}^{\text{raw}}$ is the spectrum raw signal affected by the end losses.

4 Experimental configurations

Two experimental configurations are employed to identify particular aspects of the wire performances. The wake of a heated cylinder is investigated first. The flow is set such that most of the temperature fluctuation energy appears at frequencies lower than the cut off frequency of the wire. In the second configuration, the measures are performed in the mixing layer of a heated jet for which the temperature fluctuations are distributed over a bandwidth much wider than that of the wire. For both these configurations, the center of the wire was positioned precsiely at the center of the Rayleigh scattering volume probed with the laser which remained stationary for a given set of comparative measurements. The estimated precision for the wire positioning was ±0.2 mm in all the three directions. In addition, the senstivity of the wire positioning was tested for all the measurements presented in the following

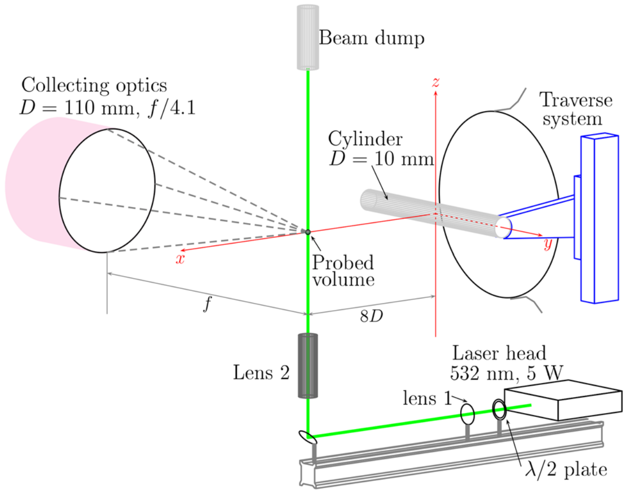

Fig. 5 Sketch of the heated cylinder configuration

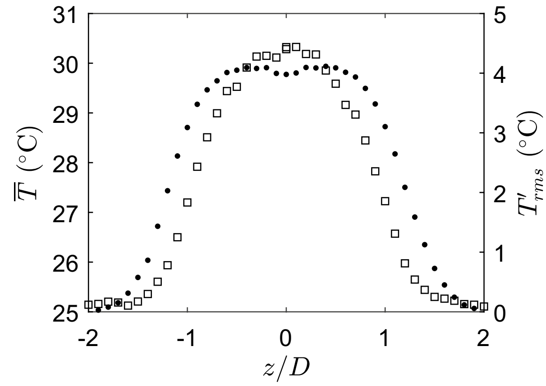

Fig. 6 Profile of the average temperature (square) and fluctuating temperature (black dot) 5D downstream of a cylinder heated at 130 °C

by moving the wire ±1 mm in the z direction without observing any significant effect on the spectra.

4.1 Heated cylinder

The experiments are performed in an open-loop low-speed wind tunnel with an exit diameter of 190 mm, providing an air flow regulated in temperature at 25 °C ± 0.2 °C by a group of resistances located at the wind tunnel air intake. A sketch of the test bench downstream of the nozzle exit is provided in Fig. 5. A cylinder with an outer diameter $D = 10$ mm and a length of 300 mm is located in the flow, 50 mm downstream of the nozzle exit. The flow velocity at the nozzle exit is $U_\infty = 5$ m/s. It corresponds to a Reynolds number based on the cylinder diameter $Re_D = 3200$. The cylinder is painted black to avoid most of the reflection affecting the optical measurements. At these low Reynolds numbers, small faults in the painted surface finish were found to strongly affect the symmetry of the wake flow. Therefore, particular care was taken to maximize the smoothness of the surface.

The brass cylinder has an inner diameter of 9 mm and is heated using 17 P1000A rectifier diodes mounted in series and sealed in an aluminium casing placed within the cylinder together with conductive heat paste. The diodes are fed by a DC power supply and serve as a heat source for the cylinder. The electrical power delivered to the diodes is around 62 W. The wall temperature taken in the downstream part of the cylinder is monitored throughout the measurements and has been found to stay within the range 130 °C ± 0.2 °C. The Richardson number Ri is equal to

$$Ri = \frac{g\frac{\Delta T}{T}D}{U_\infty^2} = 14 \times 10^{-3}, \tag{18}$$

indicating that the forced convection is dominant.

One objective of this study was to characterize the temperature fluctuations at a given axial location $x/D = 5$ downstream of the cylinder and at various locations in the transverse direction (z axis in the same figure). Because the Rayleigh scattering measurement method used here is associated with a fixed measurement point, or probed volume, with respect to the receiving optics, and because these optical components were set fixed with respect to the wind tunnel nozzle due to their weight, the decision was taken to mount the cylinder on a vertical traversing system and to determine the profiles of the temperature fluctuations by changing the vertical location of the cylinder. Preliminary measurements performed using cold wire thermometry confirmed that the results obtained by doing this are consistent with those obtained by changing the wire vertical position for a fixed position of the cylinder, within the range $z/D \in [-3;3]$, with in this case z denoting either the wire vertical position or the cylinder position. In the following, z corresponds to the vertical position of the wire with respect to the cylinder center. Profiles of the time-averaged temperature and temperature fluctuations obtained with a 1 μm wire combined with a Dantec constant current thermometer are provided in Fig. 6. This commercial thermometer does not apply any correction, so the temperature fluctuations must be regarded as an indicator to assess the main flow features, although the values are underestimated. The average temperature profile is bell-shaped and centered around the cylinder axis where the air is heated by 5 °C. The temperature fluctuations are nearly flat within $z/D \in [-0.5;0.5]$, with a slight drop near the axis similar to previous observations for similar flows (Okamoto 1988).

4.2 Hot jet

The same wind tunnel was used to set-up a co-axial jet configuration, as depicted in Fig. 7. The outer jet diameter

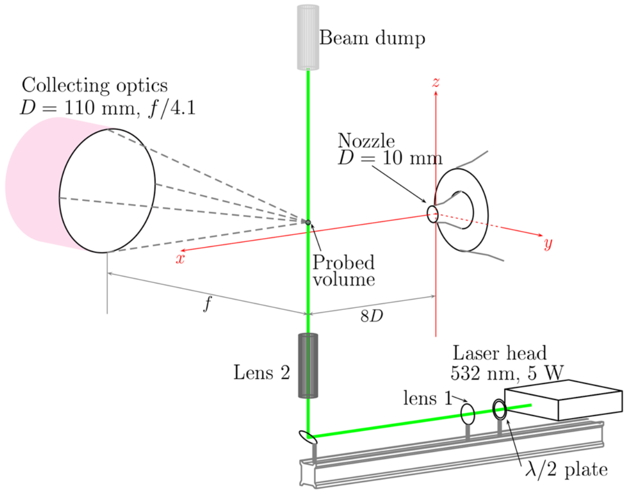

Fig. 7 Sketch of the hot jet configuration

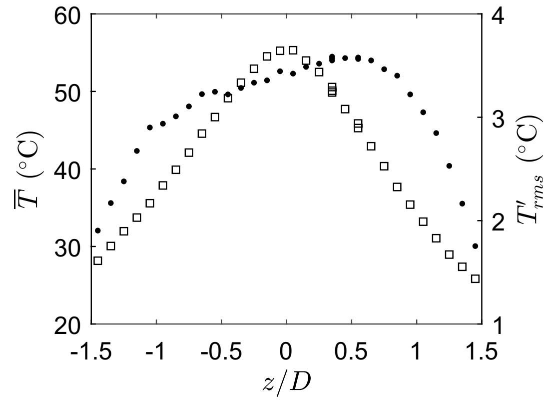

Fig. 8 Profile of the average temperature (square) and fluctuating temperature (black dot) at $x = 8D$ in a jet heated at 75°C

is 80 mm; the primary jet is heated electrically from 40 to $10D$ upstream of the nozzle exit of diameter $D = 10$ mm. The heating system uses a heated cylinder appended with fins to increase the heat transfer and inserted inside a tube of $3D$ inner diameter and $40D$ long. The nozzle contraction ratio is 9, which, with a honeycomb, facilitates the reduction of the turbulence intensity at the nozzle exit. The outer nozzle is filled with a media air filter to generate losses which reduce the exit velocity to a fraction of m/s and to generate a shear layer with the inner hot flow. This dual-flow configuration is a requirement of the Rayleigh scattering measurement technique. Indeed, Rayleigh scattering measurements must be performed in filtered flow conditions to keep the dust concentration as low as possible.

The power supply delivers 50 W to the heating system, and the jet dynamic pressure is $q = \rho_j U_j^2/2 = 58$ Pa. Under these conditions, the primary jet exit velocity is 10.9 m/s at 75 °C and hence 50 °C hotter than the secondary jet. Based on the diameter, the jet Reynolds number is $Re_D = 5800$ allowing the laminar mixing layer at the nozzle exit to quickly become turbulent. The length of the jet potential core can, therefore, be estimated to be between 4 and 5 diameters long (Lau et al. 1979). The maximum of the velocity fluctuations is expected to occur at an axial position close to twice the potential length core (Lau et al. 1979). Assuming the peak of the temperature fluctuations is close to that of the velocity fluctuations, the axial position of the measurement point was chosen at $x = 8D$. The profiles of the average and fluctuating temperature provided in Fig. 8 confirm that the maximum average temperature is significantly lower than the jet exit temperature and thus that $x = 8D$ is downstream of the potential core end. The profile of the fluctuations is rather flat near the axis, which also indicates that the jet is fully developed but surprisingly non-symmetrical. This lack of symmetry is due to a small misalignment between the heating tube and the jet axis. However, this observation will not affect the analysis in the next sections, since only the point $z = 0.6D$ that exhibits the maximum fluctuations will be considered.

4.3 Wires

For a given material, the thermal inertia of the wires mostly depends on their mass per unit length. To assess the effect of the thermal inertia compensation, two wire diameters d are considered, 1 µm and 3.1 µm. The 3.1 µm wire was bought with a diameter of 2.5 µm, but this was corrected by electron microscopy. The 1 µm wire was not measured, but the electrical resistance of the wire corresponded to the expected values. The 3.1 µm wire is mounted on four probes of different length l to vary the l/d ratio and assess the end heat loss correction proposed in Eq. (17). The characteristics of the five probes are summarized in Table 1.

The time constant $\mathscr{M}_w$ is measured by heating the wire using the same laser as for the Rayleigh scattering together with a rotating shutter to generate pulses of laser light. This technique is similar to that proposed in Weeks et al. (1988). The laser beam is focused on the shutter to reduce the rising and falling times of the light intensity to 10 µs. After the shutter, the beam is collimated with a diameter set at least twice as large as the probe length to ensure the light intensity is homogeneous all along the wire. The time constant is determined for each individual rising edge from the wire resistance time history by fitting an increasing exponential decay. The values reported in Table 1 are obtained for a velocity of 3.5 m/s by averaging the rising time of 200 edges. As expected, the rising time of the 3.1 µm probes is larger

Table 1 Main characteristics of the wires used for this study

Probe	d (μm)	l/d	Material	k_w (W/m-K)	H_p [a]	$\mathscr{M}_w$ [a] (μs)	$f_c = 1/(2\pi\mathscr{M}_w)$ [a] (Hz)	T_c (μs)
P1-0.4	1	400	Pt	71.6	0.82	53.0	3000	40.4
P3-0.4	3.1	129	W/Pt (90/10)	164	0.27	191	833	306
P3-1.25	3.1	403	W/Pt (90/10)	164	0.78	350	455	306
P3-3	3.1	967	W/Pt (90/10)	164	0.90	374	426	306
P3-6	3.1	1935	W/Pt (90/10)	164	0.95	363	438	306

[a] At 30 °C, and 3.5 m/s

than that of the 1 μm wire. However, $\mathscr{M}_w$ is surprisingly small for the shortest probe in comparison with that of the longer probes which have a similar rising time. This behavior could be an effect of the l/d ratio, but this is not observed for the other longer probes, especially for that with a length of 6 mm which has a lower time constant than the 3 mm one.

This measurement is repeated for different flow velocities between 3.5 m/s and 12 m/s. In addition, $\mathscr{M}_w$ is related in Eq. (12) to the normal flow velocity by the function $f[U]$. This function is specific to each probe, but it can be approximated by $f[U] = A_0 + B_0 U^{1/2}$, where A_0 and B_0 are two numerical coefficients (Cleve et al. 2017). Thus, $\mathscr{M}_w$ is expected to follow

$$\mathscr{M}_w = \frac{1}{A + BU^{1/2}}. \tag{19}$$

For each probe, the wire time response is fitted with Eq. (19). The results are presented for the five probes in Fig. 9. The fitted curves match well with the measurements, indicating that the model Eq. (12) is correct in the present conditions and that the time response estimation is not subject to significant random error.

The present CVA thermometer is equipped with only a few discrete values for the hardware thermal inertia compensation. Regardless of the flow velocity, the preset time constant $T_c = 40.4$ μs is that closest to the 1 μm wire probe time constant, and $T_c = 306$ μs for the four 3.1 μm wire probes.

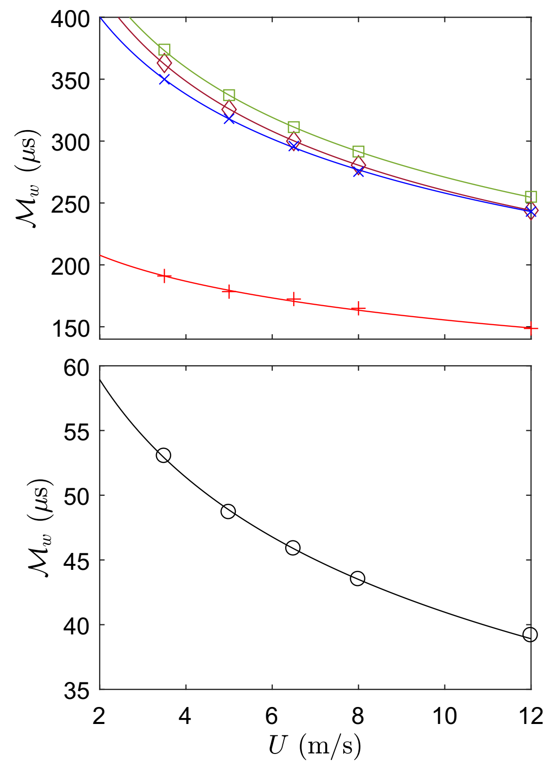

Fig. 9 Time response M_w of the probes for different normal velocities. Red plus sign P3-0.4, blue multiple sign P3-1.25, green square P3-3, purple diamond P3-6, black circle P1-0.4. Lines show the best fit based on equation (19)

5 Results

The objective of these experiments was twofold. First, the Rayleigh scattering temperature measurement method must be validated by comparison with the cold wire measurements in the low-frequency region, where thermal inertia has no effect. The validity of the Rayleigh scattering method is not frequency-dependent; therefore, showing the validity at low frequency also suggests validity at higher frequencies as long as the shot noise is not significant. Second, the thermal inertia and end loss corrections are assessed for the wires by comparison with the Rayleigh scattering measurements that serve as reference. In the following, spectra are computed from 120 s of signal sampled at 102400 Hz for the wire and 300 or 500 s of photon count-rate signals sampled at 400 kHz for the Rayleigh measurements.

5.1 Shot noise and dust contamination-induced noise floor

Rayleigh scattering measurements essentially provide fluctuations of density, or temperature in the present case. However, as mentioned in Sect. 2, for low-level fluctuations, the results are biased by shot noise and dust detections. To figure out the limits of the validity domain of the Rayleigh scattering measurements, a record was performed

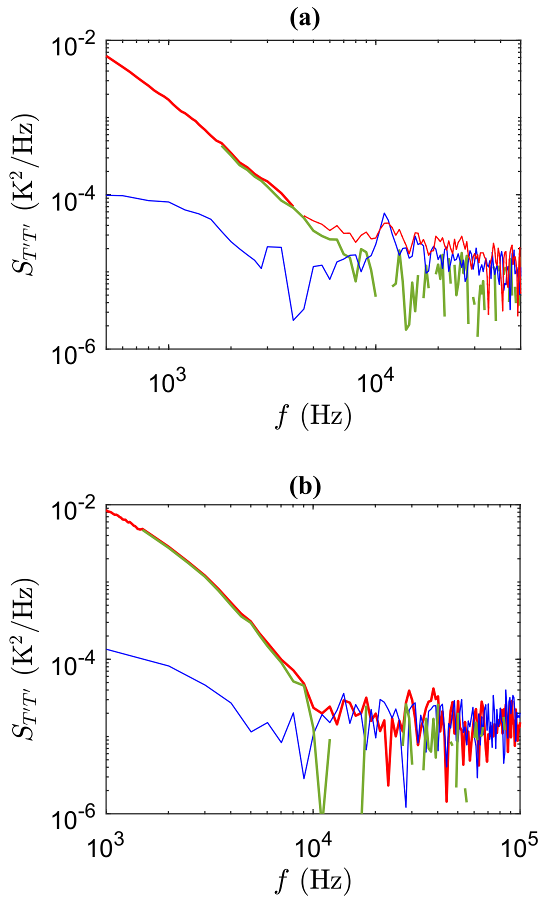

Fig. 10 Spectra of the temperature fluctuations with heating (red line), without heating (blue line), and the difference between them (green line). **a** Wake of the cylinder, **b** jet mixing layer

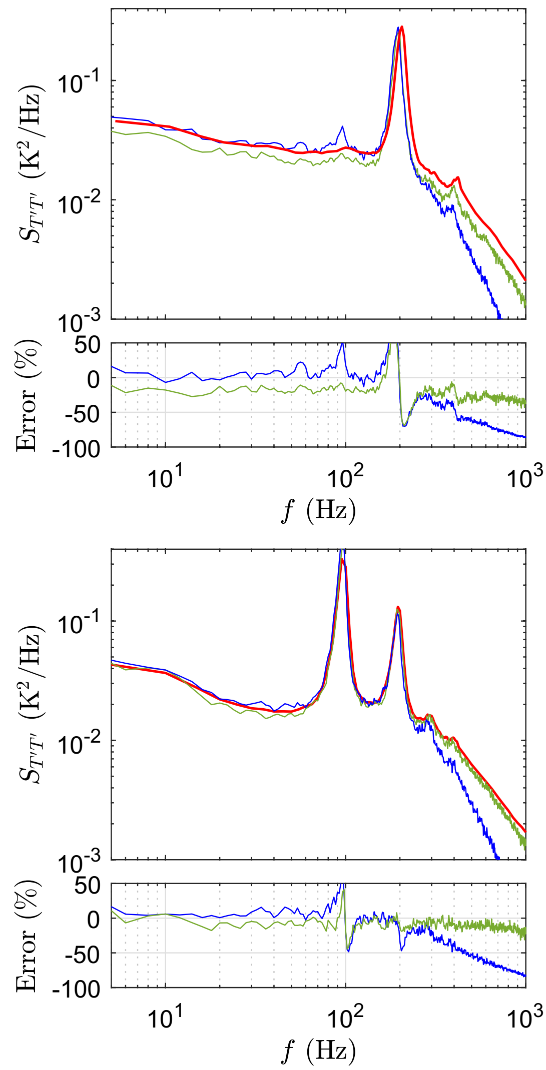

Fig. 11 Spectra of the temperature fluctuation measured by Rayleigh scattering in the wake of a cylinder at $x = 5D$ and $z = 0D$ (top)/$z = 0.5D$ (bottom) using different measurement methods without inertia correction. Red line Rayleigh, green line P1-0.4, blue line P3-1.25. Errors are relative to the Rayleigh reference

in each configuration without heating the flow. The resulting spectra only contain the contribution of the shot noise and the dust detections. They can, therefore, be used to characterize the noise floor level for temperature fluctuation measurements. The temperature fluctuation spectra are compared with these noise floor in Fig. 10 for the heated cylinder at $z = 0$, and the heated jet. A corrected temperature fluctuation spectrum obtained by subtracting the spectrum of the noise floor from the spectrum of the temperature fluctuation is plotted. This rectified spectrum is used only to assess the validity of the raw temperature fluctuation spectrum; indeed its validity can be confirmed at any frequency the correction has no effect. For the cylinder wake, the noise floor contribution can be neglected at frequencies below 4.6 kHz. This maximum achievable frequency is increased to 9 kHz for the jet mixing layer. In both cases, the contribution of the dust detections is overwhelmed by the temperature fluctuations and does not introduce any limitation; the limitation is only due to the residual shot noise level.

5.2 Low-frequency validation

At low frequencies in comparison to the probe cut-off frequencies, the effect of thermal inertia is assumed to be small. It is, therefore, possible to determine the validity of temperature measurements performed using Rayleigh scattering. In Fig. 11, the spectrum obtained by Rayleigh scattering is compared with spectra measured with the 1 µm, and the 3.1 µm probes of a l/d ratio close to 400 (P1-0.4 and P3-1.25) at $z = 0$ and $z = 0.5D$ in the wake of the heated cylinder. To facilitate the comparisons, the relative error between the cold-wires and the Rayleigh spectra is also plotted in linear scale. This test case was chosen because the temperature spectra are marked by the vortex shedding, which constitutes a good indicator for comparison between the different measures and corrections.

No thermal inertia compensation is employed for the wire measurements in Fig. 11. That is why above 200 Hz the probe P3-1.25 undergoes a rapid fall. Below 200 Hz no thermal inertia effect is observed; thus the spectra are expected to be the same for both probes. However, the energy of the fluctuations measured by the P3-1.25 probe was found to be approximately 25% above those measured by the P1-0.4 probe at $z = 0$, although only 10% error was observed at $z = 0.5D$. This discrepancy cannot be attributed to a probe positioning error, because the sensitivity to the position was tested by repeating measurements at different positions near the nominal location, and found to be very low. This error was therefore most likely due to the thermal end loss correction detailed in Sect. 3.3. This correction requires knowing the Nusselt number value, which is estimated only from the average velocity here, whereas a turbulence intensity greater than 40% was measured with a hot wire at $z = 0$.

Overall, the spectrum obtained by Rayleigh scattering was found very close to that obtained by the cold wires. In particular, all the peaks are well captured as was the weak hump below 20 Hz at $z = 0.5D$. A more precise analysis showed better agreement of the Rayleigh scattering spectrum with that obtained from both probes at $z = 0.5D$, and closer to the P3-1.25 probe at $z = 0$. However, this deviation cannot be considered as significant in view of the previous observations regarding the dependency of the spectra on the thermal end loss correction, and also of the uncertainty of ±2.4% associated with the calibration slope of the Rayleigh apparatus, corresponding to ±5.8% in spectra. The present method consisting in measuring the temperature fluctuations using a Rayleigh scattering method was validated for low-speed flows.

5.3 Effect of the thermal inertia correction

The thermal inertia correction methods discussed in Sect. 3.2 are now tested for both the flows retained. First, a nearly two-dimensional heated cylinder wake that allows using the software correction thanks to its very large spanwise integral length scale for positioning the hot and the cold wire next to each other. Second, the jet mixing layer, that contains more energy at high frequency, which prevented us from using the hot-wire based software correction because of the associated small turbulence scales.

The reference spectra and the different corrections are compared for both flows, and for the two probes with $l/d \simeq 400$ in Fig. 12. Figure 12a, b concerns the measurements performed in the cylinder wake. The low-pass filtering effect of the thermal inertia is clearly demonstrated when no correction is applied. The cut-off frequency is consistent with that provided in Table 1 from the measurements of $\mathscr{M}_{\mathrm{w}}$. Besides, the time constants set in the CVA thermometer for the hardware are smaller than the effective ones for both probes. This difference explains why the hardware correction recovers the fluctuation levels at high frequencies significantly but not perfectly.

The software correction provided results similar to the hardware correction for the 3.1 µm probe and applied a slightly weaker correction for the 1 µm probe. This method was developed for alternating flow applications, thus involving strong variations in $\mathscr{M}_{\mathrm{w}}$, and tested with success in thermoacoustics (Cleve et al. 2017). However, it did not perform better than the hardware correction in the present convective flow. This is partly because the velocity measured by the hot wire was not rigorously the same as the velocity at the cold wire station and because the values of $(m_{\mathrm{w}} c_{\mathrm{w}})/(\chi R_0)$ and $f[U]$ might have been affected by discrepancies.

The stiff software correction was based on a constant value for $\mathscr{M}_{\mathrm{w}}$, corresponding to the average flow velocity and determined from the measurements in Fig. 9. The results corrected with this method were very close to the reference over a wide frequency range. Modeling the probe by a first-order system in Eq. (10) is, therefore, satisfactory. Furthermore, the effect of the velocity fluctuations was not found to be significant for the thermal inertia correction in convected flows. Above 2 kHz, the corrected spectra start falling for both wires. Since the wires were of different lengths, this attenuation could not have been caused by the spatial averaging introduced by the size of the wires. This error may, however, have occurred because the reference measurement was overestimated in this range of frequencies. Nevertheless, Rayleigh measurements were expected to be reliable up to 4.6 kHz according to the noise floor results shown in Fig. 10 and discussed in Sect. 5.1.

Measurements in the jet mixing layer are reported in Fig. 12c, d. Similarly with the above-mentioned results, the hardware correction significantly reduced the effect of the thermal inertia. The correction was even more effective than for the cylinder wake because in the jet configuration the flow velocity was 4.5 m/s; thus the value $\mathscr{M}_{\mathrm{w}}$ decreased to a value closer to that of the CVA thermometer time constant. The larger error can be seen in Fig. 12c for the 3.1 µm probe above 3 kHz. At this frequency, the spectrum shows sharp roll-off characteristics. This resulted from the limited gain-bandwidth product of the amplifier performing the closed-loop control needed for the correction. Above this frequency the gain of the amplifier was not large enough to compensate the attenuation introduced by the thermal inertia. The maximum achievable frequency of 3 kHz is specific to this CVA thermometer, with a time constant of 306 µs. Nevertheless, this limitation is intrinsic to any thermometer offering a hardware correction functioning on the analog signal from the wire.

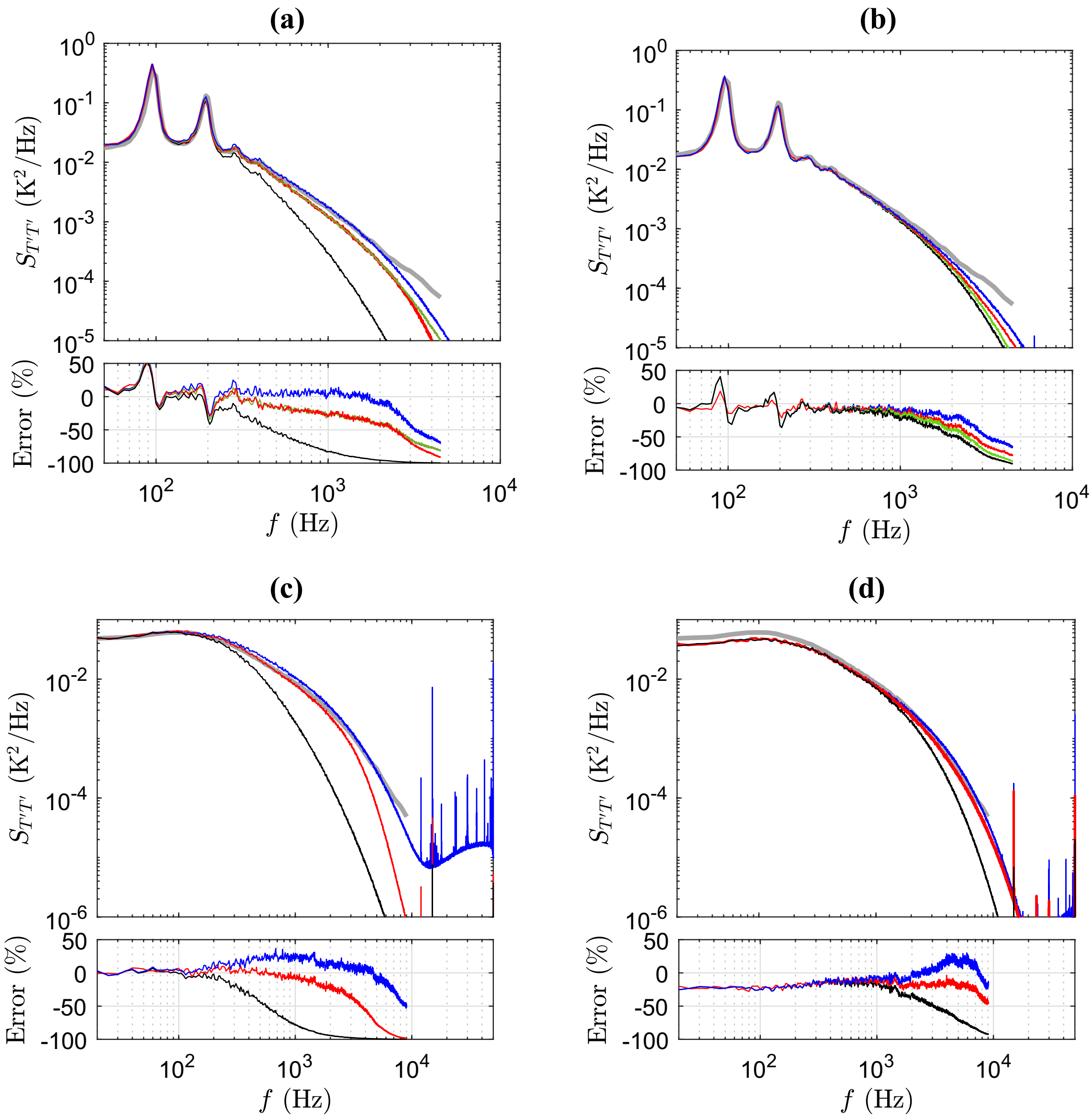

Fig. 12 **a**, **b** Temperature spectra in the wake of the heated cylinder at $x = 5D$, $z = 0.5D$. **c**, **d** Temperature spectra in the mixing layer of a hot jet at $x = 8D$, $z = 0.6D$. The P3-1.25 probe is used for (**a**, **c**), and the probe P1-0.4 for (**b**, **d**). Grey line Rayleigh, black line no thermal inertia correction, red line hardware correction, green line software correction, blue line stiff software correction. Errors are relative to the Rayleigh reference

However, for a smaller time constant, the correction would be weaker, thus the thermometer could be operated at a higher frequency.

The stiff software correction was efficient over a wider frequency range because the correction was performed numerically on the digitalized signal and was not affected by the hardware limitations.

The fluctuations were nonetheless slightly overestimated with the stiff software correction. This error was attributed to an overestimation of $\mathscr{M}_{\mathrm{w}}$ probably introduced by the uncertainty associated with the local time-averaged velocity measurement. In Fig. 12c, the effect of the correction is also clearly visible on the noise floor of the temperature fluctuation spectrum amplified at high frequency.

Figure 12d shows satisfying results for the hardware correction, and a slight overestimation of the fluctuations at high frequencies for the stiff software method. Indeed, in this configuration the inertia correction is weaker than for a 3.1 µm probe and seems to be handled well by the thermometer hardware correction up to at least 10 kHz with the time constant $T_{\mathrm{c}} = 40\,\mu\mathrm{s}$.

5.4 Effect of the end loss correction

The effect of the thermal end loss correction on the spectra was tested for the four 3.1 µm probes. Details on the correction are given in Sect. 3.3, and the values of H_p are given in Table 1 for the cylinder wake at $z = 0.5D$, which is the case considered here. Corrected spectra for all probes are compared with the reference Rayleigh spectrum in Fig. 13. For better readability, the spectra are presented against a frequency normalized by the vortex shedding frequency f_0. The first observation is the overestimation of the correction for the P3-0.4 that is larger than 60% of the reference value in the frequency range $f/f_0 < 1$. The correction factor for this probe was $H_\mathrm{p} = 0.273$. The spectra were, therefore, $1/H_\mathrm{p}^2 = 13$ times lower before the correction. The correction was so large that any uncertainty in either the model, or the wire characteristic incurred a strong error in the corrected spectra. Nevertheless a 60% error can be considered as a significant improvement in comparison with the raw results.

The spectra associated with the three remaining probes tended to collapse at low frequency. The spectrum associated with the P3-1.25 probe was very close to the reference spectrum. Spectrum associated with P3-3 and P3-6 both depicted a deficit of fluctuations above $f/f_0 = 0.2$, except near the peaks for P3-6 which almost perfectly collapsed with P3-1.25, whereas P3-3 spectrum remained lower. In addition to the thermal end losses, the effects of the spatial averaging might have had an impact on the shape of the spectrum. Indeed, long wires were of the same order of magnitude as the cylinder diameter. That might be the reason why the result for P3-1.25 was closer to the reference, and why the result for P3-6 was close to the reference only at the vortex shedding frequency characterized by a spanwise integral length scale much larger than the wire length. However, this explanation is not completely satisfactory because it does not clarify why P3-3 and P3-6 behaved similarly, whereas they have different lengths. The deficit of fluctuations observed for the P3-3 spectrum near the peaks is also questionable.

Analyzing the rms value of the fluctuations is another way of assessing the thermal end loss correction in a more global way. The rms fluctuations T'_rms were computed following Parseval's theorem within a range of frequency $[0\ f_\mathrm{max}]$ as follows:

$$T'^{\,2}_\mathrm{rms} = \int_0^{f_\mathrm{max}} S_{T'T'}\,\mathrm{d}f, \tag{20}$$

where f_max is the maximum achievable frequency with the Rayleigh scattering measurement, hence 4.6 kHz, corresponding to a Strouhal number of $St = 9.2$ based on the cylinder diameter and the flow ambient velocity. Values with and without correction are summarized in Table 2. Corrected values for T'_rms are compared with the reference ones obtained with Rayleigh scattering. The same trend for the disparities were observed with the rms values and the spectra. In the present study the best match was found with the two $l/d \simeq 400$ probes with an error lower than 3%. These probes were short enough to prevent from spatial averaging of the turbulence and long enough to keep the error introduced by the thermal end losses small.

Table 2 Temperature fluctuations in K for $f \leq 4.6$ kHz, measured in the wake of the cylinder at $z = 0.5D$ from the spectra obtained for the five cold wire probes, and for the Rayleigh measurement

Probe	T'_rms no corr.	T'_rms inertia corr.	T'_rms end /inertia corr.
Rayleigh			4.21
P1-0.4	3.31	4.05	4.11 (– 2.4%)
P3-0.4	1.53	1.61	5.89 (+ 40%)
P3-1.25	2.95	3.33	4.33 (+ 2.8%)
P3-3	2.94	3.27	3.62 (– 14%)
P3-6	3.31	3.65	3.83 (– 9.0%)

Figures in parenthesis are the errors relating to the Rayleigh value

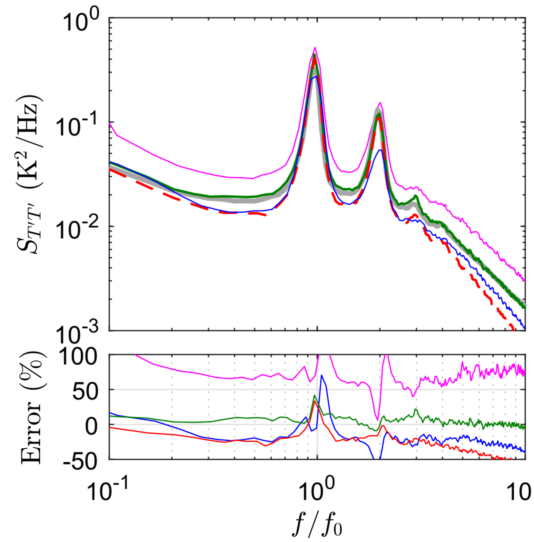

Fig. 13 Spectra of the temperature fluctuations measured in the cylinder wake at $y = 0.5D$ for probes of various l/d ratios between 2000 and 130 corrected for thermal inertia, and thermal end losses. The frequency is normalized by the vortex shedding frequency f_0. Gray line Rayleigh, red dotted line P3-6, blue line P3-3, green line P3-1.25, magenta line P3-0.4. Errors are relative to the Rayleigh reference

6 Conclusion

Temperature fluctuations were measured using CVA thermometers, and the Rayleigh scattering of light by molecules. Measurements were performed in two flows, namely in the wake of a heated cylinder, and in the mixing layer of a hot jet. The objective of this study was to assess the ability of CVA cold wire techniques to measure the temperature fluctuations beyond the cutoff frequency induced by the thermal inertia of the wires. Different inertia compensation techniques were tested, and the results were compared to the Rayleigh scattering measurements that were not subjected to inertia.

The results relating to inertia compensation showed that correction relying on modeling the wires by a time-invariant first-order low-pass filter was sufficient to perform measurements at frequencies up to 10 kHz without introducing significant errors either with a 1 µm wire, or with a 3.1 µm wire and a software correction. It was, however, necessary to first determine the wire time constant for the velocity of the flow considered.

The effect of the correction of the thermal end losses was also tested for various aspect ratios *l*/*d* of the wire and showed that the correction was overestimated if the wires were too short. Nevertheless, in the test setup, long wires also led to errors in the spectrum, probably due to spatial averaging. A value of $l/d = 400$ was found to be the best compromise between end losses and spatial extension. Further tests carried out on a larger flow scale in comparison with the size of the probes would be necessary to clearly identify the minimum *l*/*d* ratio to ensure a minimum error without introducing bias due to spatial averaging.

Acknowledgements This work was performed within the framework of the Labex CeLyA of Université de Lyon, within the program "Investissements d'Avenir" (ANR-10-LABX-0060/ ANR-11-IDEX-0007) operated by the French National Research Agency (ANR), and is also partially supported by the industrial Chair ADOPSYS co-financed by SAFRAN-SNECMA and ANR (ANR-13-CHIN-0001-01).

References

Antonia RA, Browne LWB, Chambers AJ (1981) Determination of time constants of cold wires. Rev Sci Instrum 52(9):1382–1385
Berson A, Poignand G, Blanc-Benon P, Comte-Bellot G (2010) Capture of instantaneous temperature in oscillating flows: Use of constant-voltage anemometry to correct the thermal lag of cold wires operated by constant-current anemometry. Rev Sci Instrum 81(1):015102
Bruun HH (1995) Hot-wire anemometry: principles and signal analysis. Oxford University Press, New York
Cleve S, Jondeau E, Blanc-Benon P, Comte-Bellot G (2017) Cold wire constant voltage anemometry to measure temperature fluctuations and its application in a thermoacoustic system. Rev Sci Instrum 88:044904
Collis DC, Williams MJ (1959) Two-dimensional convection from heated wires at low reynolds numbers. J Fluid Mech 6(3):357–384
Comte-Bellot G, Weiss J, Béra JC (2004) Lead-resistance effects in a constant voltage anemometer. Rev Sci Instrum 75(6):2075–2081
Denos R, Sieverding CH (1997) Assessment of the cold-wire resistance thermometer for high-speed turbomachinery applications. J Turbomach 119(1):140–148
LaRue JC, Deaton T, Gibson CH (1975) Measurement of high-frequency turbulent temperature. Rev Sci Instrum 46(6):757–764
Lau JC, Morris PJ, Fisher MJ (1979) Measurements in subsonic and supersonic free jets using a laser velocimeter. J Fluid Mech 93(1):1–27
Mangalam AS (2018) Real-time, high-bandwidth measurement of large amplitude velocity and temperature fluctuations using constant voltage anemometry. In: 2018 Aerodynamic measurement technology and ground testing conference, pp AIAA–2018–2991
Mercier B (2017) Development of a method for density measurements by Rayleigh scattering to be applied to jet noise study, and contribution to study of screech in underexpanded jets. Ph.D. thesis, Université de Lyon, 2017LYSEC61
Mercier B, Castelain T, Bailly C (2018a) Experimental investigation of the turbulent density—far-field sound correlations in compressible jets. Int J Aeroacoust 17(4–5):521–540
Mercier B, Castelain T, Jondeau E, Bailly C (2018b) Density fluctuations measurement by Rayleigh scattering using a single-photomultiplier. AIAA J 56(4):1310–1316
Okamoto A (1988) Influence of sound waves on flow and heat transfer around heating cylinder (translated from japanese). J Heat Transfer Soc Jpn 27(107):84–97
Panda J (2016) A molecular Rayleigh scattering setup to measure density fluctuations in thermal boundary layers. Exp Fluids 57(12):183. https://doi.org/10.1007/s00348-016-2267-9
Panda J, Gomez C (2003) Setting up a Rayleigh scattering based flow measuring system in a large nozzle testing facility. In: 9th AIAA/CEAS Aeroacoustics Conference, Hilton Head, South Carolina, pp AIAA–2003–1089
Panda J, Seasholtz R, Elam K (2005) Investigation of noise sources in high-speed jets via correlation measurements. J Fluid Mech 537:349–385
Panda J, Seasholtz RG (2002) Experimental investigation of density fluctuations in high-speed jets and correlation with generated noise. J Fluid Mech 450:97–130
Penelet G, Leclercq M, Wassereau T, Picart P (2016) Measurement of density fluctuations using digital holographic interferometry in a standing wave thermoacoustic oscillator. Exp Therm Fluid Sci 70:176–184
Sohn KH (1991) Experimental study of boundary layer transition with elevated freestream turbulence on a heated flat plate. Ph.D. thesis, Case Western Reserve University
Tsuji T, Nagano Y, Tagawa M (1992) Frequency response and instantaneous temperature profile of cold-wire sensors for fluid temperature fluctuation measurements. Exp Fluids 13(2):171–178
Weeks A, Beck J, Joshi M (1988) Response and compensation of temperature sensors. J Phys E Sci Instrum 21(10):989